https://doi.org/10.1016/j.psep.2021.12.039

An integrated computational strategy for the geometric design and prioritization of wave-plate mist eliminators

Ya Tang[1,3], YuTing Xu[1,3], BingJian Zhang[2,3], Chang He[2,3]*, QingLin Chen[2,3]*, Jingzheng Ren[4]

1. School of Chemical Engineering and Technology, Sun Yat-Sen University, Zhuhai, 519082, China;
2. School of Materials Science and Engineering, Sun Yat-Sen University, Guangzhou 510275, China;
3. Guangdong Engineering Center for Petrochemical Energy Conservation, The Key Laboratory of Low-carbon Chemistry & Energy Conservation of Guangdong Province, Guangzhou 510275, China
4. Department of Industrial and Systems Engineering, The Hong Kong Polytechnic University, Hong Kong Special Administrative Region, China

Submitted to *Process Safety and Environmental Protection*

*Corresponding authors: Chang He, E-mail addresses: hechang6@mail.sysu.edu.cn.

QingLin Chen, E-mail addresses: chqlin@mail.sysu.edu.cn.

Abstract:

In this study, a computational strategy is proposed for geometric design and prioritization of wave-plate mist eliminators by combining the Taguchi experimental design, CFD modelling, and Fuzzy Analytic Hierarchy Process (FAHP) approaches. The Taguchi approach is first used to identify a balanced set of geometric parameters and to generate 16 design cases depending on the chosen levels. A batch of CFD runs is then performed on these design cases to obtain the detailed multi-phase flow behaviour. Finally, the FAHP approach is employed in assisting the multi-criteria decision-making process of these design cases based on multi-run CFD results. To probe the separation mechanism, five design cases (named Cases 4, 8, 12, 15, and 16) with relatively high graded mean integration representation scores (GMIRs=0.0819, 0.0774, 0.0814, 0.0784, 0.0780) are systematically compared and analyzed regarding the profiles of static pressure, velocity, turbulent kinetic energy, etc. It indicates that Case 4, with the maximum level of bends (n=4) and dimensionless width (W/S=0.55), as well as the minimum wavelength of a bend (λ=1), can effectively reduce the power consumption while achieving a higher separation efficiency.

Keywords: wave-plate mist eliminator; prioritization; Taguchi experimental design; Fuzzy Analytic Hierarchy Process; power consumption; separation efficiency

1 Introduction

The increasing need for water-saving and pollution control has generated great interest in designing highly-efficient mist eliminators in industrial thermal processes. There are several types of mist eliminators such as wave-plates, filters, vanes, wire mesh (Liu et al. 2017). Among them, wave-plate mist eliminators, which basically consist of a series of narrowly spaced curved plates which are most widely used for capturing the escaping liquid droplets and restricting fog plume generation. A vital factor that influences the separation performance is the specific geometry of the flow channel, *i.e.* the channel width, the bend angle and wavelength, the number of stages (Koopman et al., 2014; Fang et al. 2021). Many mist eliminators are also equipped with drainage plates (hooks) in positions where the re-entrainment from the liquid film may occur and the deposited droplets may accumulate. Besides, some types of intensification measures such as staggered tube banks were adopted in the mist eliminators aiming at removing fine droplets at higher efficiencies.

Generally, the increased geometrical complexity can promote separation efficiency but inevitably comes at the cost of pressure drop and energy comsumption due to the increased fluid turbulence dissipation. In this case, the development of prediction and optimization models is vital to assist the decision-making of the design and operation of a practical demister. For example, Zhao et al. (2007) developed a surrogate model of separation efficiency of the demisters based on the response surface method. Narimani and Shahhoseini (2011) constructed a prediction model for the separation efficiency of

a vane demister using CFD modelling and statistical methods. Yu et al. (2021) bulit a correlation for predicting pressure drop and separation efficiency of demisters coupled with the cooling tower system. Note that, to obtain more realistic results, the prediction models constructed by multi-phase CFD simulation must track the interaction and spatial movement of each particle by solving large-scale distributed partial differential equations. In addition, the construction of optimization models would involve a great number of CFD tasks in the design space, which are costly and time-consuming. Consequently, the accuracy of these models must be weighed against the computational burden to construct them, which becomes a major driver and impedes in developing better mist eliminator designs.

The design of experiment (DoE) is a well-suited approach to reduce computational resources and time, as it can maximize the amount of process information obtained from a finite size of calculations by properly selecting experimental points (Wissmann and Grover, 2010). The traditional DoE approaches such as sequential experimental design (Schwaab et al., 2006), full factorial design (Gottipati and Mishra, 2010), and Taguchi experimental design (Feng et al., 2020) have been widely applied in identifying the main effects of geometric factors. Although when using these applications, it is hard to handle multi-criteria or multi-objective process cases using traditional DoE approaches. Moreover, note that the commonly used evaluation criteria for a demister, such as pressure drop, collection efficiency, energy use, Euler number, impact factor, etc., are inter-related or even competing in most cases. In this regard, the traditional DoE should

be combined with a proper multi-objective criterion to assist such complex decision-making for the prioritization of various designs.

The Analytic Hierarchy Process (AHP) proposed by Thomas Saaty (1977) is an effective tool for organizing and evaluating alternative solutions based on mathematics and psychology (Wang and Yeap, 2021). By reducing complex decisions to a series of pairwise comparisons and synthesizing the results, it can provide a comprehensive and rational framework for structuring a decision problem, which helps to capture both subjective and objective aspects of a decision (Ooi et al., 2018). Nevertheless, it is often controversial because human qualitative judgments often have the characteristics of ambiguity and intangibility. Besides, the fuzziness and vagueness existing in many decision-making problems may contribute to the imprecise judgments of decision-makers (Ahn, 2017). To overcome the weakness of the AHP, the Fuzzy-AHP (FAHP) method that combines fuzzy theory and the AHP technique has been introduced in a multi-criteria decision-making process (Ogundoyin and Kamil, 2020). As an extension of Saaty's theory, it adopted the interval ratio judgments to elicit the decision-maker preferences instead of adhering to precise ratio judgments. Due to its more sufficient description of the decision-making compared with AHP, FAHP has been implemented by many researchers for application in different domains.

In this study, an integrated computational strategy is developed by combining experimental design, CFD modelling, and FAHP scheme for achieving the better geometric design of wave-plate mist eliminators. To ensure high efficiency in the

operation of a mist eliminator in a wide design space, a manageable set of experiments is first generated based on a Taguchi orthogonal array. The detailed behaviour of multi-phase airflow inside mist eliminators for all design cases is achieved by performing a batch of two-dimensional CFD simulations. Besides, the droplet separation efficiency and the associated pressure drop for all design cases are used as performance indicators to prioritize the design cases with a comprehensive performance utilizing FAHP. Finally, a preferred combination of geometric parameters is confirmed by analyzing the flow behaviour of the design cases.

2 Computational Strategy

In the proposed solution strategy, three rigorous design and evaluation approaches are combined to identify the optimal wave-plate mist eliminators. As shown in Fig. 1, it starts with the experience and knowledge of the wave-plate mist eliminators from plant engineers and researchers, which provide information regarding the process setting of baseline design and evaluation criteria. The Taguchi experimental design is first used to determine a balanced set of geometric parameters among the effective factors and to generate a manageable size of design cases (experiments). After that, a batch of CFD runs is carried out on the generated design cases to obtain the detailed flow behaviour of a multi-phase inside mist eliminators, as well as the objectives of separation efficiency and pressure drop for each design case. In the final step, the FAHP method is employed for multiple comparisons of the evaluation criteria and for e.

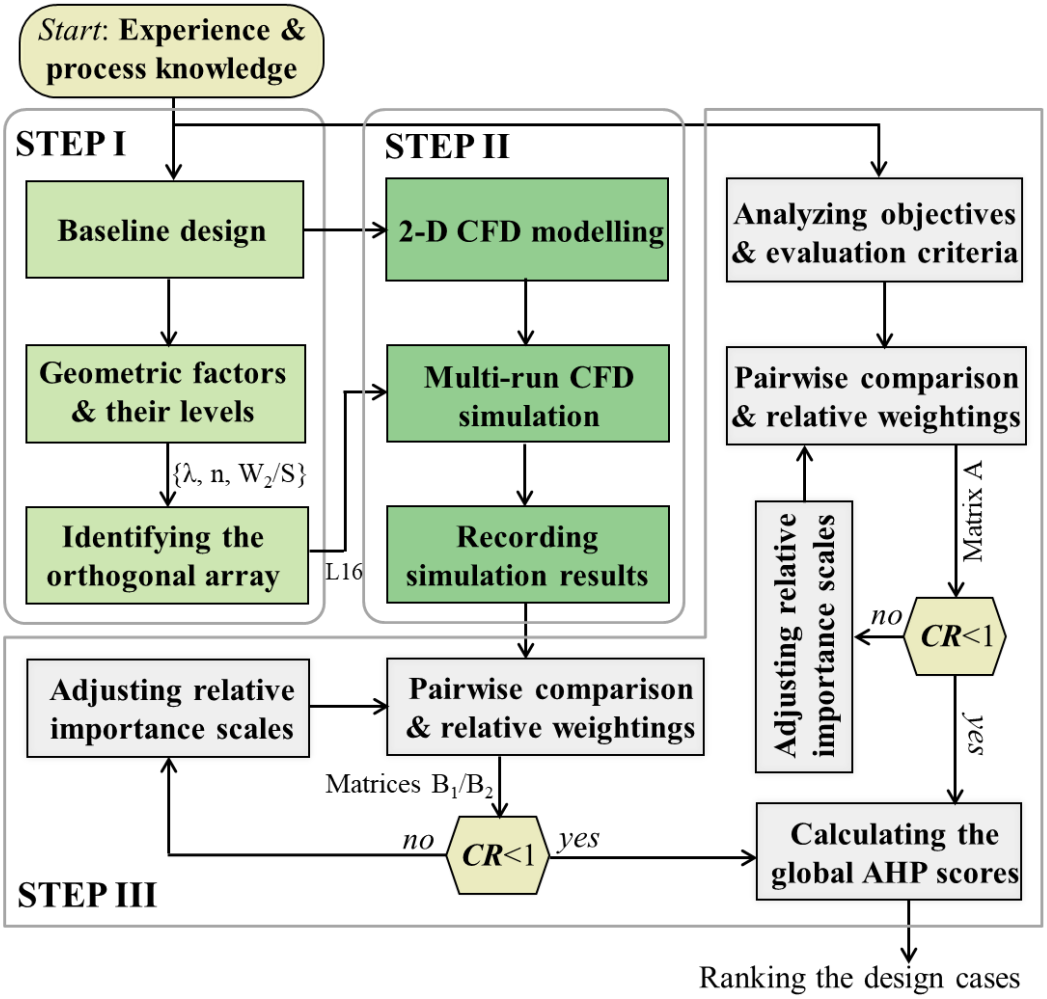

Fig. 1: Flowchart of the combined Taguchi-CFD-FAHP strategy. STEP I: Taguchi experimental design, STEP II: CFD modelling and STEP III: FAHP.

2.1 Taguchi experimental design

The Taguchi experimental design follows a procedural approach where the design of a baseline case (Tang et al., 2021) is first analyzed. Fig. 2 presents a two-dimensional sketch of this baseline case with two bends. As shown, the gas flow carrying droplets passes through a series of channels that have sharp bends and drainage plates. The liquid droplets which cannot rapidly change direction due to the inertia, deviate from the main gas flow and adhere to the channel walls, where they form liquid rivulets that can be drained out from the demister (Galletti et al., 2008). In this way, the concentration of

liquid droplets of the airflow would decrease after passing through the mist eliminator. According to the sensitivity analysis in the literature (Estakhrsar and Rafee, 2016; Kavousi et al., 2013), three key parameters, including λ, dimensionless width (W_2/S), and bends number (n), played a more important role in affecting the overall performance of the wave-plate mist eliminator. To reduce the computational costs and improve the design efficiency, these three parameters are selected in the experimental design. The basic geometric parameters such as the wavelength of a single bend (**λ**), the channel width (S), and the distance between the drainage plate and demister's wall (W_2), etc., are also provided in this figure. On this basis, three key parameters (including **λ,** dimensionless width W_2/S, and bends number n) and four representative levels for the selected geometric parameters are considered in the experimental design.

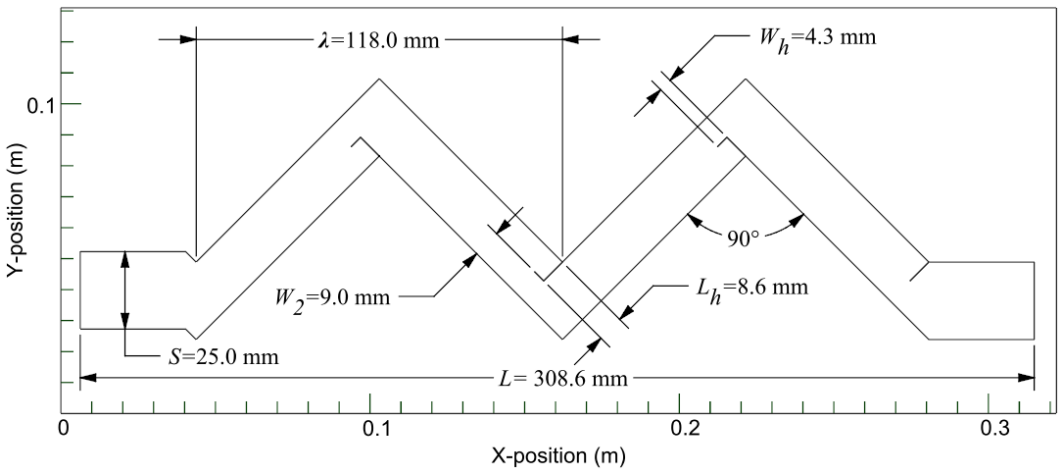

Fig. 2: Two-dimensional sketch of the baseline case. The symbols of the basic geometric parameters are provided in the Nomenclature.

The main purpose of the orthogonal array is to identify a finite size of design cases with irrelevant and non-overlapping information, so that it can represent the entire

design space. As listed in Table 1, an orthogonal array of 16 cases for 3 parameters with 4 levels is first identified in this study. The rigorous CFD simulation of the mist eliminator is then carried out for each of the designs in the orthogonal array, as detailed in Section 3. The recorded simulation results that include separation efficiency and pressure drop of these 16 design cases can be further used as inputs for determining the optimal designs by using the FAHP method.

Table 1 The orthogonal array of 16 cases for 3 parameters with 4 levels

No.	Levels of the parameters			No.	Levels of the parameters		
	λ	n	W_2/S		λ	n	W_2/S
1	1 (60 mm)	1 (1)	1 (0.25)	9	3 (180 mm)	1	3
2	1	2 (2)	2 (0.35)	10	3	2	4
3	1	3 (3)	3 (0.45)	11	3	3	1
4	1	4 (4)	4 (0.55)	12	3	4	2
5	2 (120 mm)	1	2	13	4 (240 mm)	1	4
6	2	2	1	14	4	2	3
7	2	3	4	15	4	3	2
8	2	4	3	16	4	4	1

2.2 Two-dimensional CFD modelling

To describe the two-dimensional air-water flow inside a mist eliminator, the main assumptions are as follows: (1) the continuous phase gas flow with the constant property is incompressible due to the low flow velocity; (2) the droplets (modelled as hard spherical particles) do not rebound into the gas flow since they are collected and removed as soon as they impinge on the channel walls (Xu et al., 2017); (3) The

mechanisms of droplet-droplet interaction, droplet break-up, or the splash of impinging droplets are not taken into account; (4) a one-way coupling is applied to simulate the effects of droplets on the gas flow and (5) there is no interactive phase change or heat transfer between the gas flow and the droplet.

2.1.1 Governing equations

The computational model of two-dimensional mist eliminators, including the continuity, momentum, and turbulence equations, is carried out by solving Reynolds-averaged Navier-Stokes (RANS) equations. Compared to other methods such as direct numerical simulation, it retains the model accuracy with the least computational burden in most industrial applications in particular for two-dimensional CFD modelling. The equations of continuity and momentum can be written as:

$$\frac{\partial u_i}{\partial x_i} = 0 \tag{1}$$

$$\rho\left(\frac{\partial u_i}{\partial t} + \frac{\partial u_i u_j}{\partial x_j}\right) = -\frac{\partial P}{\partial x_i} + \mu\frac{\partial^2 u_i}{\partial x_j^2} + \mu\frac{\partial^2 u_j}{\partial x_i \partial x_j} - \rho\frac{\partial \overline{u_i' u_j'}}{\partial x_j} \tag{2}$$

where u_i and u_j are the fluid Reynolds average velocity components, P is the fluid pressure, ρ is the fluid density. In this equation, $\overline{u_i' u_j'}$ is known as the Reynolds stress tensor that arises from RANS equations. The effects of turbulence on the mean flow have been incorporated in RANS turbulence models via $\overline{u_i' u_j'}$, whilst providing closure to the system of equations (Fadhila et al., 2020).

The SST κ-ω turbulence model is a two-equation eddy-viscosity model that is the

most commonly used in CFD to describe the mean flow characteristics for turbulent flow conditions (Odu et al., 2016; Pinilla et al., 2020). The SST formulation also switches to a κ-ε behaviour in the free-stream and thereby avoids the common κ-ω problem that the model is too sensitive to the inlet free-stream turbulence properties. In this work, the SST κ-ω turbulence model is used to simulate the turbulent flow in the mist eliminator. A general description of turbulence using two transport equations of the SST κ-ω model is expressed as (Xie et al., 2019):

$$\frac{\partial}{\partial t}(\rho\kappa)+\frac{\partial}{\partial x_i}(\rho\kappa u_i)=\frac{\partial}{\partial x_i}(\Gamma_\kappa^{'}+\frac{\partial\kappa}{\partial x_i})+G_\kappa-Y_\kappa+S_\kappa \tag{3}$$

$$\frac{\partial}{\partial t}(\rho\omega)+\frac{\partial}{\partial x_j}(\rho\omega u_j)=\frac{\partial}{\partial x_j}\left(\Gamma_\omega^{'}\frac{\partial\omega}{\partial x_j}\right)+G_\omega-Y_\omega+D_\omega+S_\omega \tag{4}$$

where Y_κ and Y_ω are the turbulence energy dissipation rates of κ and ω; D_w is the orthogonal diffusion term; G_κ is the turbulent kinetic energy due to the velocity gradient, and G_ω is the production of the specific dissipation ω; S_κ and S_ω are the source terms of κ and ω; Γ_κ and Γ_ω are the effective diffusivities of κ and ω, and their definitions are given as:

$$\Gamma_\kappa=\mu+\frac{\mu_t}{\sigma_k} \tag{5}$$

$$\Gamma_\omega=\mu+\frac{\mu_t}{\sigma_\omega} \tag{6}$$

where σ_κ and σ_ω are the Prandtl numbers of κ and ω; μ_t is the turbulent viscosity; μ is the fluid molecular viscosity.

The Discrete Phase Model is employed in this work to simulate the gas-liquid contact process by tracking a large number of droplets, whose acting force equilibrium equation of droplets motion could be expressed by (Xie et al., 2017; Zhu et al., 2020):

$$\frac{dv_p}{dt} = F_D(v_g - v_p) + \frac{g_x(\rho_p - \rho_g)}{\rho_p} + F_x \tag{7}$$

where $F_D(v_g\text{-}v_p)$ represents the drag force of the unit mass particle, F_x is an additional acceleration term that mainly includes thermophoretic force and Brownian motion force (Xu et al., 2017). Since $\rho_p \gg \rho_g$ in the calculations, the terms of forces due to gravity, pressure and added mass can be negligible to simplify numerical simulation (Zamora and Kaiser, 2011).

$$F_D = \frac{3\mu C_D Re_p}{4\rho_P D_P^2} \tag{8}$$

where D_p is the particle diameter; Re_r is the Relative Reynolds number of the particle, which can be expressed as (Bae et al., 2020):

$$Re_r = \frac{\rho_g D_p \left|\overrightarrow{v_g} - \overrightarrow{v_p}\right|}{\mu} \tag{9}$$

C_D is the drag coefficient, which can be given as follows:

$$C_D = a_1 + \frac{a_2}{Re_r} + \frac{a_3}{Re_r^2} \tag{10}$$

where coefficients a_1, a_2 and a_3 are constants given by Morsi and Alexander (1972).

2.2.2 Turbulent dispersion

In this study, the dispersion of droplets due to turbulence in the gas phase is predicted by adopting the Discrete Random Walk (DRW) model. This is because the DRW model can account for the effect of instantaneous turbulent velocity fluctuations on the droplet trajectories by applying stochastic methods (Gao et al., 2017). Each turbulent eddy is characterized by Gaussian probability distributed random velocity fluctuations (u', v', w') and a time scale (τ_e). By computing the trajectory for a sufficient number of representative particles, the random effects of turbulence on the particle dispersion may be simulated. The fluctuating term u_i' that prevails during the particle-eddy interaction time can be written as (Li et al., 2020):

$$u_i' = \xi\sqrt{\overline{u_i'^2}} \tag{11}$$

where ξ is a normally distributed random number. The random velocity fluctuation u' is kept constant over a certain integration time, which depends on the characteristic time scale or eddy characteristic lifetime τ_e. The integration time can be regarded as the fluid Lagrangian time scale T_L as the particles are fine enough. The eddy characteristic lifetime is defined as:

$$\tau_e = 2T_L = 2C_L\frac{k}{\varepsilon} \tag{12}$$

where C_L is an integral time-scale constant ranging from 0.1 to 0.96 (Tian and Ahmadi, 2007); For the κ-ω models, substitute $\omega=\varepsilon/\kappa$ into Eq. (21). As reported by Kavousi (2013), the change of C_L (normally ranging from 0.16 to 0.25) has very limited effect

on the simulation results; herein it is set to 0.2 for calculating the integral time scale.

2.2.3 Mesh and boundary conditions

The numerical grid contains a finer near-wall mesh in the mist eliminators' wall surfaces, with the first grid point located at 0.13 mm away from the wall that evolves to the core region with a growth factor of 1.02 in the normal direction. Adopting these settings, the domain was later meshed with quadrilateral cells to form an unstructured mesh (see Fig. 3a). The quantity and quality of the mesh system are of great importance in improving the accuracy and reducing the time of simulations. Three different kinds of grid systems (coarse grid with the interval size of 0.8 mm, middle grid with the interval size of 0.5 mm, and fine grid with the interval size of 0.3 mm) are generated and compared to ensure that the results are independent of the grid size. Under the same operating conditions, the turbulent kinetic energies at X=0.07 m and 0.17 m are acquired by three grid systems as shown in Fig. 3(b-1) and (b-2). The calculation solution obtained by the middle grid is extremely close to that of the fine one with much less computational burden. This comparison indicates that the middle mesh with a grid number of 32,600 is acceptable considering the convergent time and solution precision.

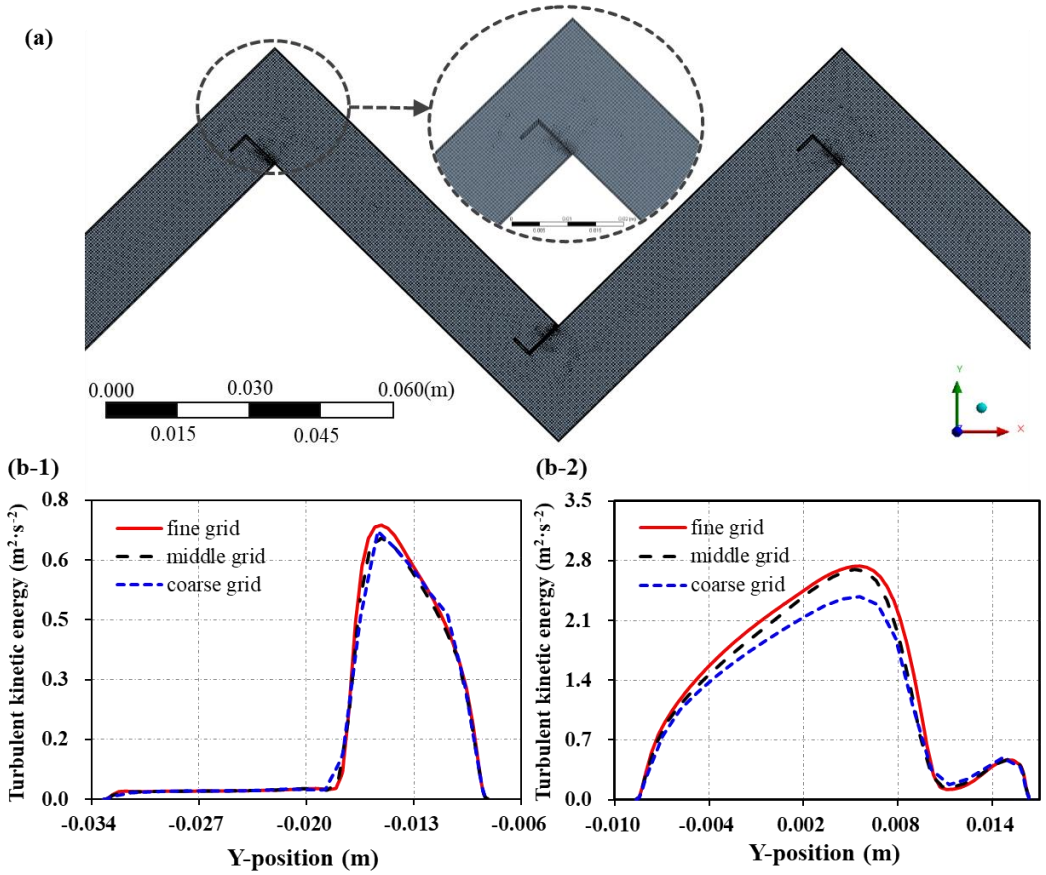

Fig. 3: (a) Generated mesh system for CFD computation and the profiles of turbulent kinetic energy using different grid sizes at: (b-1) X= 0.07 m; (b-2) X= 0.17 m.

The CFD software ANSYS FLUENT 2019R1 (2019) was applied for the present numerical simulation. The governing equations with their boundary conditions are solved by using the SIMPLEC algorithm. This is mainly because of the increased under-relaxation that can be applied during the iteration process (Ansys, 2019). With SIMPLEC, there is no need to under-relax the pressure-correction (the default under-relaxation factor is set to 1.0), which contributes to a 20-30% speed-up in convergence.

Meanwhile, the under-relaxation factors remain as the default since there is no unstable or divergent behaviour observed during the iteration process. The second-order up-wind differencing scheme is chosen for convective terms to offer a more accurate

finite difference stencil for the approximation of the spatial derivative. The solution is considered to be converged when all the scaled residuals are less than 10^{-5} for all governing equations and turbulence quantities. If the convergence is not achieved to the desired accuracy when computations reached a steady state, the iteration is continued further to a stage. In this stage, the solution is considered to be converged when the results do not vary even after 500 iterations (Venkatesan et al., 2013). For the continuous phase, the velocity inlet is employed since the inlet velocity is constant and its direction is perpendicular to the boundary. At the wall, zero heat flux and no-slip conditions are imposed. The pressure-outlet boundary condition with a default value is adapted to its outlet. As the droplet reaches the wall, it is assumed the droplet is captured and removed from the gas flow. Besides, the airflow with a density of ρ_g=1.225 kg·m^{-3} and viscosity of μ_g=1.789×10^{-5} Ns·m^{-2}, as well as the gas velocity ranging from 2 to 4 m·s^{-1} are employed in the numerical simulation. The detailed boundary conditions of the numerical model can be found in Table S-1 in the Supporting Information (SI).

2.3 Fuzzy set and FAHP

2.3.1 Fuzzy set theory

The fuzzy set theory is a mathematical tool to address the imprecision and uncertainty that is inherent in human judgment in the decision-making process through the use of linguistic terms and degrees of membership (Ren et al., 2020). A fuzzy number is a convex fuzzy set characterized by a given interval of real numbers, and the

membership function satisfies a series of conditions. In this study, a special class of fuzzy numbers, namely Triangular fuzzy numbers (TFNs), is used to express the decision-maker's comprehensive performance evaluation for the mist eliminators. The mathematical membership function $\mu_{\tilde{\theta}}(x):\mathbb{R}\to[0,1]$ that is defined for the TFNs $\tilde{\theta} = (l,\ m,\ u)$ is as follows.

$$\mu_{\tilde{\theta}}(x)=\begin{cases}(x-l)/(m-l), & l\le x\le m\\ (u-x)/(u-m), & m\le x\le u\\ 0, & \text{otherwise}\end{cases} \tag{13}$$

where l, m, and u are the lower, median, and upper values of the TFNs, respectively, which are often employed to illustrate the fuzziness of the data evaluated. The basic fuzzy arithmetic operation principles of two triangular fuzzy numbers can be found in the literature.

2.3.2 FAHP method

The FAHP method shown in Step III in Fig. 1 consists of a series of consecutive procedures. Firstly, all the evaluation criteria of interest in the decision-making process should be carefully analyzed. Note that, the relative weighting between the evaluation criteria is generally subjective and thus differs from designer to designer according to the experience and knowledge. As for designing a mist eliminator, increasing the separation efficiency of droplets is always a priority in practice. Under the premise of satisfactory separation efficiency, the designers will seek the pressure drop of the mist eliminator to be as low as possible for the sake of energy saving. Thus, it is considered

that separation efficiency is a relatively more important criterion than pressure drop.

In FAHP, the reference comparison between the evaluation criteria is described as linguistic terms (i.e. absolutely important, very important, equally important, etc.). The transformation rules of linguistic terms to show the relative importance of each pair of factors in a similar hierarchy are listed in Table S-2 in the SI. On this basis, a fuzzy comparison matrix **A** that contains the linguistic terms is constructed by pairwise comparison between the two evaluation criteria of a mist eliminator. Following the same procedure, the other two matrices $\mathbf{B}_1$ and $\mathbf{B}_2$, containing linguistic measures for the relative significance of each pair of design cases with respect to a specific criterion are constructed, as detailed in Tables S-3 and S-4 in the SI.

Once the comparisons are completed, the matrix that only contains the results of linguistic terms, is converted into fuzzy members by the defined fuzzy scale. After that, the TFN is defuzzified into a crisp numerical value via graded mean integration representation (GMIR) (Guo and Zhao, 2017). Suppose $\tilde{\theta} = (l, u, m)$ is a triangular fuzzy number, the defuzzified crisp number is given by

$$\tilde{\theta}_{crisp} = \frac{l + 4m + u}{6} \tag{14}$$

The generated crisp matrices are shown in Tables S-5 and S-6 in the SI. The pairwise matrices are normalized using Eq. (3).

$$x_{ij,norm} = \frac{x_{ij}}{\sum_{i=1}^{n} x_{ij}} \tag{15}$$

where $\sum_{i=1}^{n} x_{ij}$ is the sum of the elements in the column.

The eigenvector of the matrix which presents the relative crisp weightings of the criteria ($w_{i,crisp}$) or the design cases ($c_{i,crisp}$) for a specific criterion (Ogundoyin and Kamil, 2020) can be calculated by:

$$w_{i,crisp} \text{ or } c_{i,crisp} = \frac{\sum_{j=1}^{n} x_{ij,norm}}{n} \tag{16}$$

where n is the number of criterion or design case and $w_{i,crisp}$ or $c_{i,crisp}$ is the eigenvector in row i.

The largest eigenvalue of the crisp matrix can then be computed by:

$$\lambda_{max,A} = \sum_{i=1}^{n} \left\{ \left(\sum_{j=1}^{n} x_{ij} \right) \times w_{i,crisp} \right\} \tag{17}$$

$$\lambda_{max,B} = \sum_{i=1}^{n} \left\{ \left(\sum_{j=1}^{n} x_{ij} \right) \times c_{i,crisp} \right\} \tag{18}$$

where $\lambda_{max,A}$ and $\lambda_{max,B}$ are the largest eigenvalues of matrices A and B_1/B_2, respectively.

The consistency check can be achieved by adopting the consistency ratio as expressed by (Aguilar-Lasserre et al., 2009):

$$CR_A = \frac{\lambda_{max,A} - n}{RI(n-1)} \tag{19}$$

$$CR_B = \frac{\lambda_{max,B} - n}{RI(n-1)} \tag{20}$$

where CR_A and CR_B are the consistency ratios of matrices A and B_1/B_2, respectively; RI

is the random index (Saaty, 1977).

The pairwise comparison procedure must be repeated until the consistency of the matrix is acceptable, generally CR_A or CR_B <0.1. On this basis, the next step is to calculate the criteria weightings (w_i) or the local weightings of design cases (c_i) by using the fuzzy synthetic extent analysis approach (Deng, 1999):

$$w_i \text{ or } c_i = \sum_{j=1}^{n} \tilde{x}_{ij} \otimes [\sum_{i=1}^{n} \sum_{j=1}^{n} \tilde{x}_{ij}]^{-1} \tag{21}$$

where $\tilde{x}_{ij} = (x_{ij}^{l}, x_{ij}^{m}, x_{ij}^{u})$ and $\sum_{j=1}^{n} \tilde{x}_{ij}$ can be obtained by performing a fuzzy addition operation. That is:

$$\sum_{j=1}^{n} \tilde{x}_{ij} = (\sum_{j=1}^{n} x_{ij}^{l}, \sum_{j=1}^{n} x_{ij}^{m}, \sum_{j=1}^{n} x_{ij}^{u}) \quad \forall j \in [1, 2,...,n] \tag{22}$$

The expression of $[\sum_{i=1}^{n} \sum_{j=1}^{n} \tilde{x}_{ij}]^{-1}$ can be obtained by executing the inverse operation.

$$[\sum_{i=1}^{n} \sum_{j=1}^{n} \tilde{x}_{ij}]^{-1} = (\frac{1}{\sum_{j=1}^{n} x_{ij}^{u}}, \frac{1}{\sum_{j=1}^{n} x_{ij}^{m}}, \frac{1}{\sum_{j=1}^{n} x_{ij}^{l}}) \quad \forall j \in [1, 2,...,n] \tag{23}$$

The fuzzy estimates of the criteria weightings and local weightings of design cases are presented in Table S-7 in the SI. Adding the local weighting per design case multiplied by the weighting of the corresponding criterion, a global fuzzy weighting is obtained for each design case. Finally, by ordering the global GMIRs of the fuzzy weightings for all design cases, a final case ranking can be obtained.

3 Results and Discussion

For all of the 16 design cases, the droplet separation efficiency and pressure drop

are investigated to evaluate the overall performance of the mist eliminators. The droplet separation efficiency (or removal efficiency, η) of the mist eliminator in the numerical simulation is expressed as the percentage of droplets captured by the mist eliminator to the total droplets released from the inlet, which can be calculated according to:

$$\eta = \frac{\text{number of trapped droplets}}{\text{number of entering droplets}} \times 100\,\% \tag{24}$$

The quality or the performance of a wave-plate mist eliminator is assessed by its ability in water droplet separation efficiency and pressure drop across the mist eliminator. However, improving the separation performance of water droplets normally implies that the inlet gas flow has to undergo a higher pressure drop as it passes through the mist eliminator. That is, the separation efficiency is increased at the expense of consuming more fan power. Therefore, a trade-off between the separation efficiency and pressure drop is essential in an actual mist eliminator design.

3.1 Model validation

The overall separation efficiency of the wave-plate mist eliminator is used to test the reliability of the developed numerical model by comparing it with the experimental results (a maximum uncertainty below 5%) obtained from Ghetti et al. (2003). The demister is formed by four bends, with a total length of 0.2925 m and a pitch of 0.025 m. The liquid droplets are generated by the two-fluid ultrasonic nozzle with the droplet size ranging from 2 to 70 μm and a Sauter mean diameter of 7.9 μm. To present a fair comparison, the numerical results were obtained under the same operating conditions.

The inlet gas velocity used in model validation is set as 2.0 $m \cdot s^{-1}$ with the diameter size ranging from 3.41 to 19.91 μm. As shown in Fig. 4, compared to SST κ-ω without the DRW model, the SST κ-ω with the DRW model is capable of providing a more accurate prediction of the flow in the mist eliminator with a small discrepancy between the numerical and experimental results. In particular, the advantage of SST κ-ω with the DRW model in prediction capability is obvious in the range of low droplet diameters, e.g. as D_p=6.23 μm, the discrepancy of the separation efficiency by using SST κ-ω with the DRW model is only 2.49%, while it drastically increases to 52.4% when using SST κ-ω without DRW. This could be attributed to the fact that the inclusion of the effect of DRW on turbulent droplet dispersion significantly improves the accuracy of describing the turbulent flow of air in the wave-plate mist eliminator.

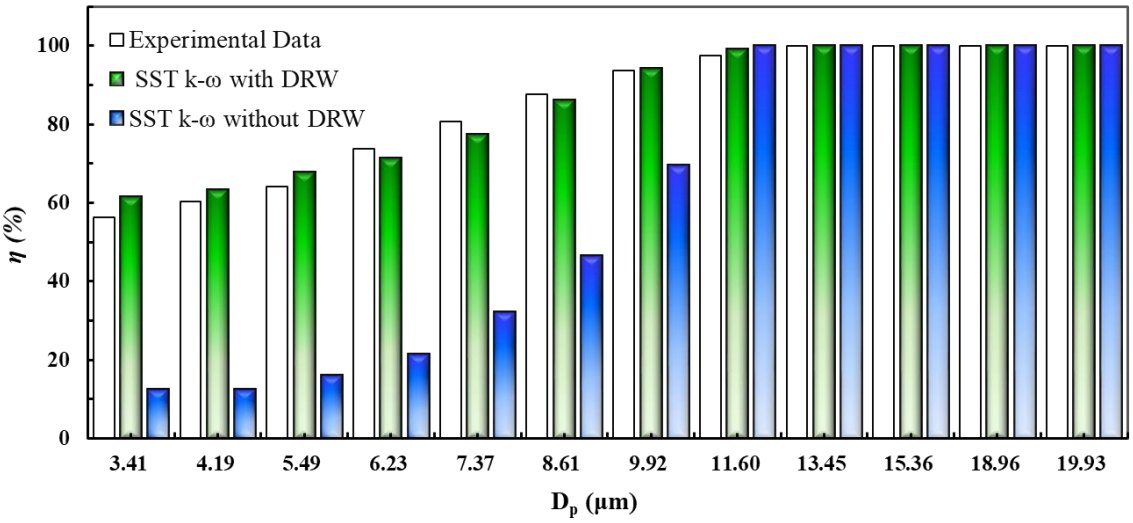

Fig. 4: Comparison of the separation efficiencies obtained from experiment and CFD simulation (SST κ-ω *w/wo* DRW).

3.2 Separation efficiency and pressure drop

Fig. 5a shows the droplet separation efficiency of the wave-plate mist eliminators at the inlet velocity of 2.0 $m \cdot s^{-1}$ and droplet diameter of 6.0 μm. It can be observed that Cases 4 , 6, 11, 12, and 16 show an almost 100% separation efficiency, which are 93.66%, 95.18%, 97.67%, 98.84% and 99.82%, respectively. This indicates that almost all fine droplets entering the mist eliminator are trapped. Note that, Cases 6, 11 and 16 have the lowest level of dimensionless width, which indicates that the hook ends are near the adjacent wall and produce the narrowest flow region. This causes the majority of droplets to impact the wall of the hook when passing through the narrow area. Besides, Cases 3, 8 and 15 have moderate separation efficiencies which are 82.32%, 82.86%, and 91.25%, respectively. The lowest separation efficiency, only 27.23%, is found in Case 9. Besides, the pressure drop of the airflow across the mist eliminator is a great concern for the mist eliminator designers since it is directly proportional to the power consumption and operational cost of the cooling tower. As shown in Fig. 5b, the highest pressure drop is observed in Case 16 with a value of 624.4 Pa where the drainage plate is very close to the adjacent wall. By contrast, the design of Case 9 leads to the lowest pressure drop (39.8 Pa) which is almost 6.4% compared with Case 16.

Fig. 5c shows the fuzzy weightings of all design cases and Fig. 5d further shows the calculated GMIR scores for these cases selected by the Taguchi experimental design. It is clear that the GMIR scores of Cases 4 and 12 take the lead with values of 0.0819 and 0.0814, followed by the results of Case 15 (0.0784), Case 16 (0.0780), and Case 8 (0.0774). This means that the overall performances of these design cases are superior

to that of rivals. For example, Case 5 has the lowest global score (0.0411), which is around half of Case 4 (0.0819). Based on the results of GMIR scores, in the following sections, we only investigate the flow fields of Cases 4, 8, 12, 15, and 16, as well as the baseline case for a more detailed comparison.

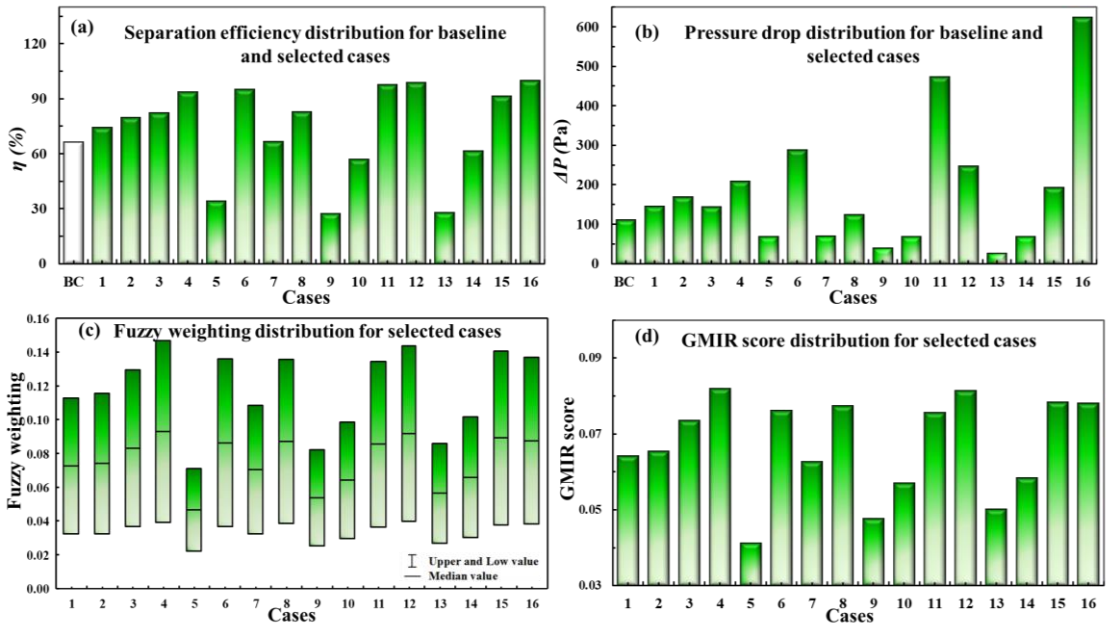

Fig. 5: Distributions of (a) η, (b) ΔP, (c) Fuzzy weighting, and (d) GMIR scores for all cases of the mist eliminator. BC is the abbreviation for the baseline case.

3.3 Contours of static pressure, velocity, kinetic energy, and droplets

The contours of static pressure within the computational domains are numerically analysed under an inlet velocity of 2.0 $m \cdot s^{-1}$. As shown in Fig. 6, it is very clear that for all investigated cases there is a jump in the operating pressure profile as the curved hook end forms a narrow gap with the concave surface of the curved wave plate. This could be due to the airflow separation from the sharp corners of the hook. Among the cases investigated, it is observed that the baseline case has the lowest pressure drop with a

peak value of only 110.9 Pa. By contrast, the highest pressure drop of 624.4 Pa across the wave plate is observed in Case 16, which is nearly 5.6 times higher than that of the baseline case. Besides, Cases 12 and 15 produce great pressure drops (246.5 Pa and 192.4 Pa) across the mist eliminators, which are almost 2.22 and 1.73 times higher than that of the baseline case, respectively. This is mainly due to the joint effect of the increased flow resistance, a large number of bends, and the low distance between the hook and the inner wall, which causes a strong distortion in the air-flow direction and reduces the flow areas in the flow channel.

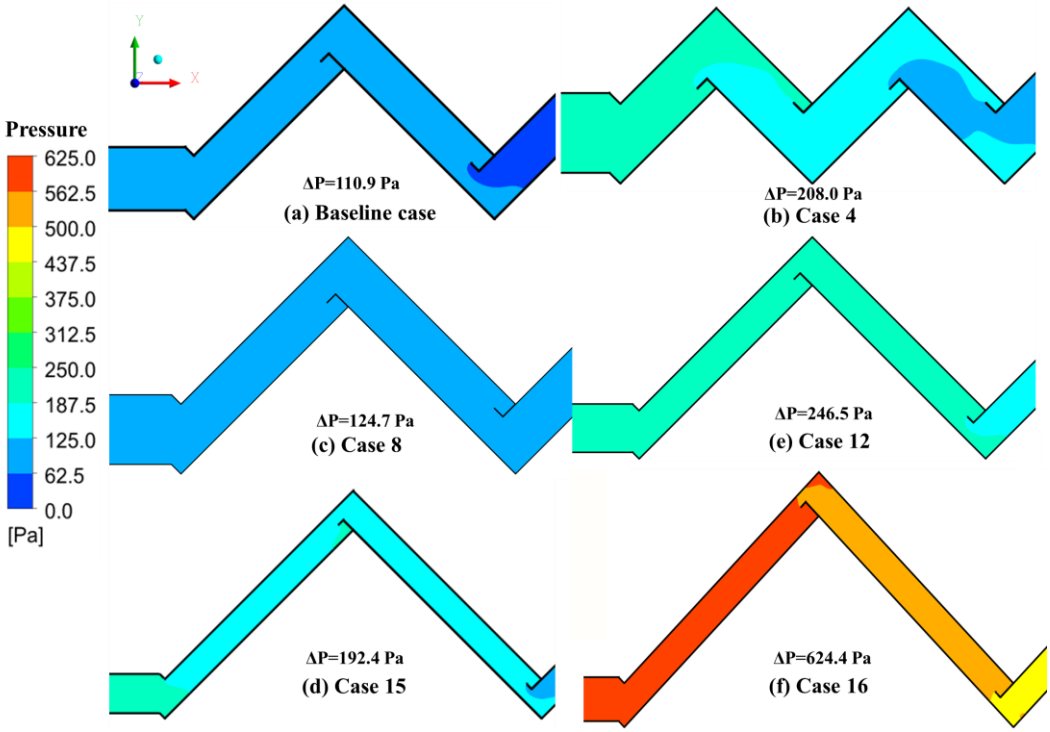

Fig. 6: Contours of static pressure in the flow domain for the selected cases at the inlet gas velocity of 2.0 $m \cdot s^{-1}$.

Fig. 7 shows the velocity contours of the gas flow for all investigated cases at the

inlet gas velocity of 2.0 $m \cdot s^{-1}$. Note that, the fluid region that is close to zero velocity indicates there is a flow recirculation due to the adverse wall pressure gradient formed by the strong geometric curvature. It is seen that Case 16 has the highest velocity profile with a maximum value of 12.77 $m \cdot s^{-1}$ appearing near the hook plate, which is almost 1.44 times greater than that of the baseline case. This is simply because Case 16 with the lowest level of W_2/S has a small spacing between the hook and mist eliminator inner surface, which causes a strong curvature and a high fluid velocity near the hook plate. Behind Case 16, Case 4 has the second-highest velocity profile within the flow domain with a peak value of 11.20 $m \cdot s^{-1}$ in the narrowest region, followed by Case 12 (9.1 $m \cdot s^{-1}$).

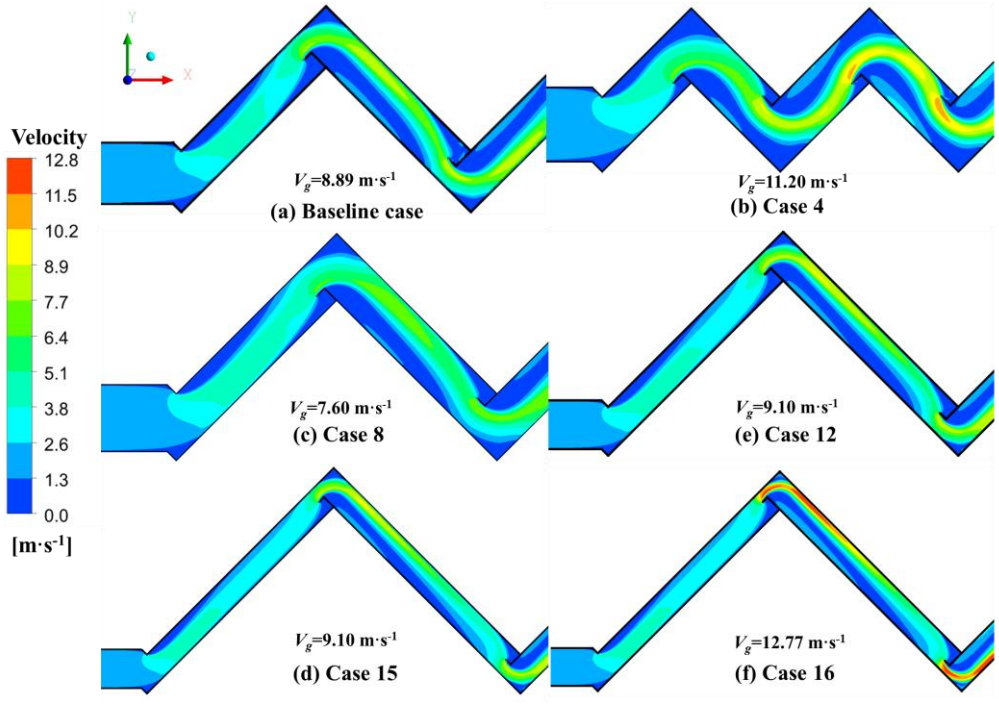

Fig. 7: Contours of velocity magnitude in the flow domain for the selected cases at an inlet velocity of 2.0 $m \cdot s^{-1}$.

It is interesting that in Fig. 7a, the baseline case with a large W_2/S has the highest velocity magnitude of 8.89 $m \cdot s^{-1}$ in the flow domain, which is almost 4.5 times higher than the average velocity, although it is the lowest one compared with other cases. While the flow domain of the mist eliminator with a high-velocity profile would bring larger inertial force to the droplets and make them more likely to separate from the gas flow, it generally comes at a high energy consumption. Therefore, an excessively high-velocity magnitude in the mist eliminator is not desirable in the design process.

To better understand the separation mechanism, it is essential to study the turbulent kinetic energy profile in the flow domain of the wave-plate mist eliminator. For all cases shown in Fig. 8, it is seen that the turbulent kinetic energy of Case 4 takes the lead with a peak value of 6.9 $m^2 \cdot s^{-2}$, which appeared at the sharp turn as the inlet velocity is 2.0 $m \cdot s^{-1}$. By contrast, the baseline case has a considerably lower turbulent kinetic energy profile with a peak value of 3.75 $m^2 \cdot s^{-2}$, which is only 54.35% of Case 4. Besides, the fine droplets in the baseline case are more likely to be entrained in the outlet by the airflow. In particular, it is easier for the fine droplets to hit the inner wall and be trapped under a higher turbulent kinetic energy. To conclude, a high value of turbulent kinetic energy with a relatively low-pressure drop would contribute to improving the overall performance of the design of the mist eliminator.

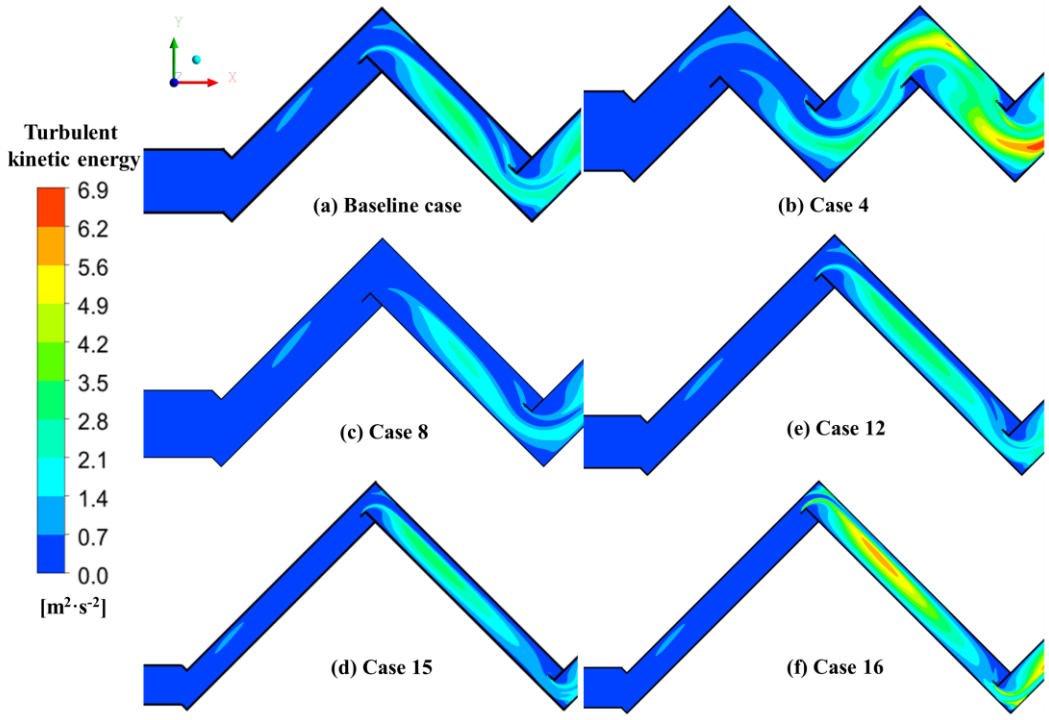

Fig. 8: Contours of turbulent kinetic energy in the flow domain for the selected cases at an inlet gas velocity of 2.0 $m \cdot s^{-1}$.

The trajectories of fine droplets in the flow domains for all investigated cases with the same number of droplets injected at an inlet gas velocity of 2.0 $m \cdot s^{-1}$ are shown in Fig. 9. Due to the lowest level of dimensionless width (W_2/S=0.25), the fine droplets in Case 16 compulsorily have to pass through the stenotic region in the flow domain, where they are more likely to hit the inner wall of the mist eliminator and detach from the airflow. Accordingly, the trajectories of the fine droplets in these cases are chaotic and disordered, making it difficult for the droplets to escape from the mist eliminator's outlet. Although the trajectories of droplets are relatively uniform and smooth, Case 4 also has the lowest level of wavelength of a single bend, as well as two successive 90° bends. This geometry leads to a strong curvature and increases the probability for the

droplets to impinge on the walls of the wave and drainage plates. The results indicate that the geometric parameters, especially the dimensionless width and the wavelength, would severely affect the droplet trajectory that leads to changes in the separation efficiency of a practical mist eliminator.

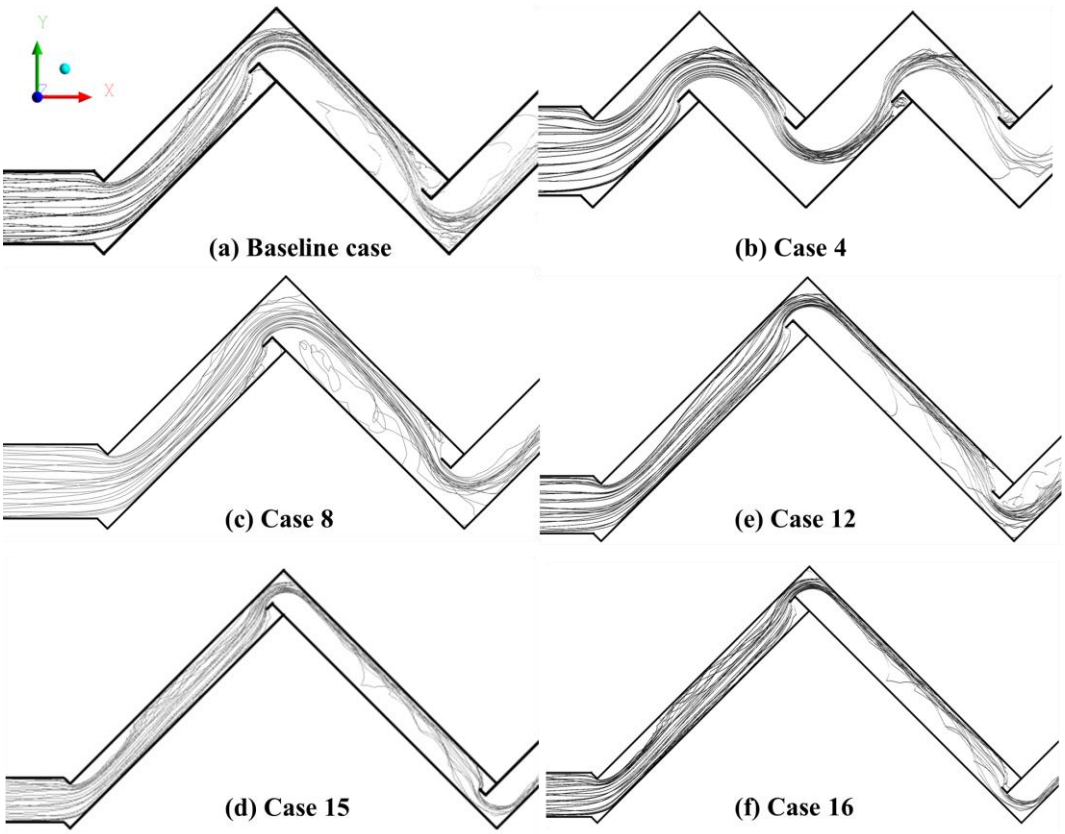

Fig. 9: Droplet trajectories in the flow domain for the selected case studies at an inlet velocity of 2.0 $m \cdot s^{-1}$.

3.4 The influence of droplet diameter and gas velocity

The separating ability of the cases investigated is explored at varied droplet sizes (3.4~13.5 μm). As shown in Fig. 10a, for all cases the separation efficiencies show an upward trend with the rise in droplet size just before approaching the perfect separation

efficiency (η=100%). The descending order of the critical droplet sizes that correspond to the perfect separation is as follows: baseline case (13.5 μm) > Cases 8 and 15 (11.6 μm) > Cases 4 (8.6 μm) > Cases 12 and 16 (7.4 μm). Among them, Case 12 stands out due to its high and stable level of separation ability, e.g. the separation efficiency of this case only increases by about 4.6% from 95.4% to 100% as the droplet diameter rises from 3.4 μm to 8.6 μm. By contrast, the baseline case with the largest size of critical droplet is very sensitive to the change in droplet size, which has the highest increase in separation efficiency by 32.5% from 54.7% to 87.2% within the same range of droplet diameters. This highlights that the baseline case has the lowest separating ability compared with other investigated cases.

Fig. 10(b) further compares the separation efficiencies and pressure drops of the investigated cases over a wide range of gas velocities (2.0~4.0 $m \cdot s^{-1}$). As shown on the left axis, the separation efficiencies for Cases 4, 8, 15, and the baseline case start with an increase to a certain extent, but the increasing rates quickly slow down with a further rise in the inlet gas velocity due to the presence of fully developed turbulence in the flow domain. Besides, the separation efficiencies of Cases 16 and 12 are remarkably high and not sensitive to the change of the inlet gas velocity throughout the given range. Note that, the separation efficiency of the baseline case is much lower than that of rivals, e.g. to obtain a perfect separation efficiency of 100%, Case 4 only requires an inlet gas velocity of 2.0 $m \cdot s^{-1}$, while for the baseline case the required inlet gas velocity is approximately doubled to 4.0 $m \cdot s^{-1}$.

On the right axis of Fig. 10b, the pressure drop of investigated cases is compared to better understand the restriction of applying high gas velocities. Overall, it is evident that the pressure drop increases steadily with the rise in inlet gas velocity, especially for Case 16. Under the gas velocity of 2.0 $m \cdot s^{-1}$, the ranking of the pressure drops is as follows: Case 16 (624.4 Pa)> Cases 12 (246.5 Pa)> Case 4 (208 Pa)> Cases 15 (192.4 Pa) > Cases 8 (124.7 Pa) > baseline case (110.9 Pa). Besides, the gaps of pressure drop between these cases become more apparent under a higher airflow rate. This phenomenon can be explained by the larger energy dispersion brought about by the higher gas velocity when interacting with the channels of the mist eliminator. Besides, note that Case 16 has the highest pressure drop (2.55 KPa), followed by Case 12 (1.03 KPa) at the inlet gas velocity of 4 $m \cdot s^{-1}$. This can be attributed to the fact that the low level of W_2/S in these cases considerably reduces the effective flow area, and hence augments the flow resistance and produces a much higher pressure drop.

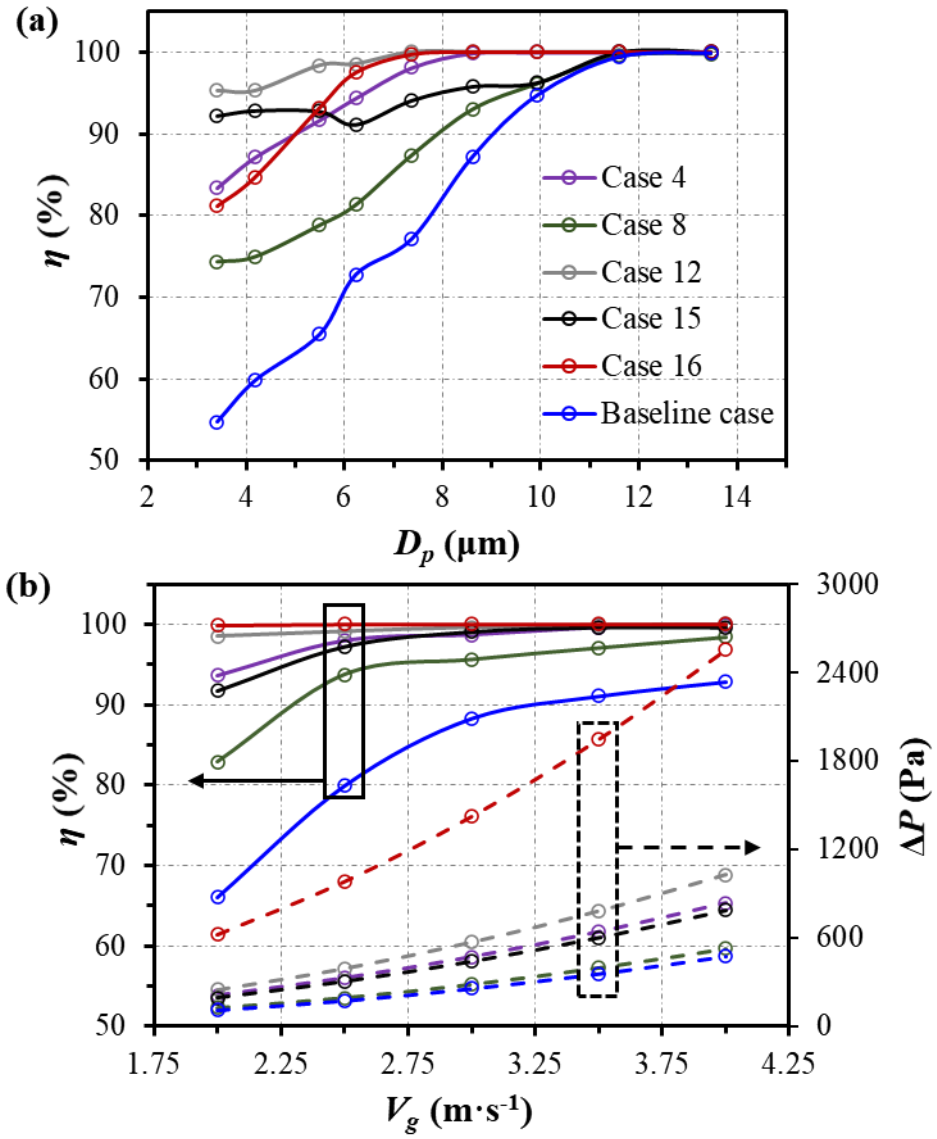

Fig. 10: (a) the separation efficiencies for various droplet diameters; (b) the separation efficiencies and pressure drops for various gas velocities.

The dimensionless pressure drop coefficient C_{pl} is an important indicator of the average resistance in the process of the gas flow across the mist eliminator, as defined by:

$$C_{pl} = 2\frac{\Delta p}{\rho_g v_g{}^2} \tag{25}$$

Table 2 lists the dimensional pressure drop coefficients under varied Reynolds numbers. Due to the increased geometric complexity, Case 16 has the highest average pressure drop coefficient with a peak value of 240.8 compared with other cases. By contrast, the baseline case with the simplest geometry has the lowest average pressure drop coefficient (C_{pl}=42.4), which is only 17.6% of Case 16. This indicates that the increased geometrical complexity could result in a higher pressure drop coefficient. Besides, as an inherent property of the mist eliminator, note that the dimensional pressure drop coefficient is only determined by the geometric parameters of the mist eliminator and thus is independent of the operating parameters. As a result, it remains approximately constant as the Reynolds number varies for all the design cases.

Table 2 The pressure drops and coefficients under various Reynolds numbers*.

	Re (1.0×10^3)	C_{pl}		Re (1.0×10^3)	C_{pl}
Baseline case	2.8	41.7	Case 4	1.4	81.8
	3.9	42.2		1.8	81.7
	4.4	43.4		2.6	81.2
Case 8	2.6	46.3	Case 12	2.2	91.5
	3.2	47.9		2.9	93.9
	4.4	46.8		3.7	95.8
Case 15	2.3	73.3	Case 16	1.8	235.7
	3.0	74.1		3.5	242.0
	3.9	75.0		4.4	244.7

* $Re = S\rho_g v_g / \mu_g$

3.5 Energy consumption

A well-designed mist eliminator should consider the evaluation criteria from both high separation ability and low energy cost in practical application. As mentioned previously, for a given size of the droplet, perfect separation efficiency will be achieved by raising the gas velocity to a high enough level. That is, a higher gas velocity is more beneficial to the improvement in separation efficiency. Nevertheless, this improvement comes at a greater pressure drop, and consequently an additional energy expenditure. Therefore, further attention is focused on investigating the energy cost of the selected design cases. According to Zamora and Kaiser (2011), a variable that is proportional to the power of intake fans can be defined as $\text{Power}_{fans} \propto \Delta p \times v_g$. In this study, due to $\Delta p \propto C_{pl} \times \text{Re}^2$ and $v_g \propto St$, a dimensionless coefficient, ζ, denoting the power consumption can be written as:

$$\zeta = \frac{\Delta p S^2 \rho_g}{\mu_g^2} \times St \tag{26}$$

where St is the Stokes number, which can be expressed as:

$$St = \frac{\rho_p D_p^2 v_g}{18 \mu_g S} \tag{27}$$

For each design case and droplet diameter, the magnitude of variable ζ depends on the required separation efficiency that is mandatory to reach. Herein, the corresponding optimal values of the power consumption and Reynolds number are represented by $\zeta_{\min}$ and $Re_{\min}$, respectively. As shown in Fig. 11, for all the design cases, the $\zeta_{\min}$ shows a

declining trend with the increase of the dimensionless droplet diameter. This trend in turn indicates that for relatively small droplets, a high ζ_{min} is expected to achieve the desired separation efficiency since increasing the inlet gas velocity has a positive impact on removing droplets from the gas flow. Meanwhile, Case 4 presents a lower ζ_{min} under a wide range of D_p/S. On the contrary, Case 16 has the highest ζ_{min} in the same range, which is almost 5.3 and 9.6 times higher than that of Case 4 as D_p/S=3.2×10^{-4} and 4.0×10^{-4}, respectively. This reflects the power consumption can be reduced by adopting an appropriate design of the mist eliminator in a cooling tower application.

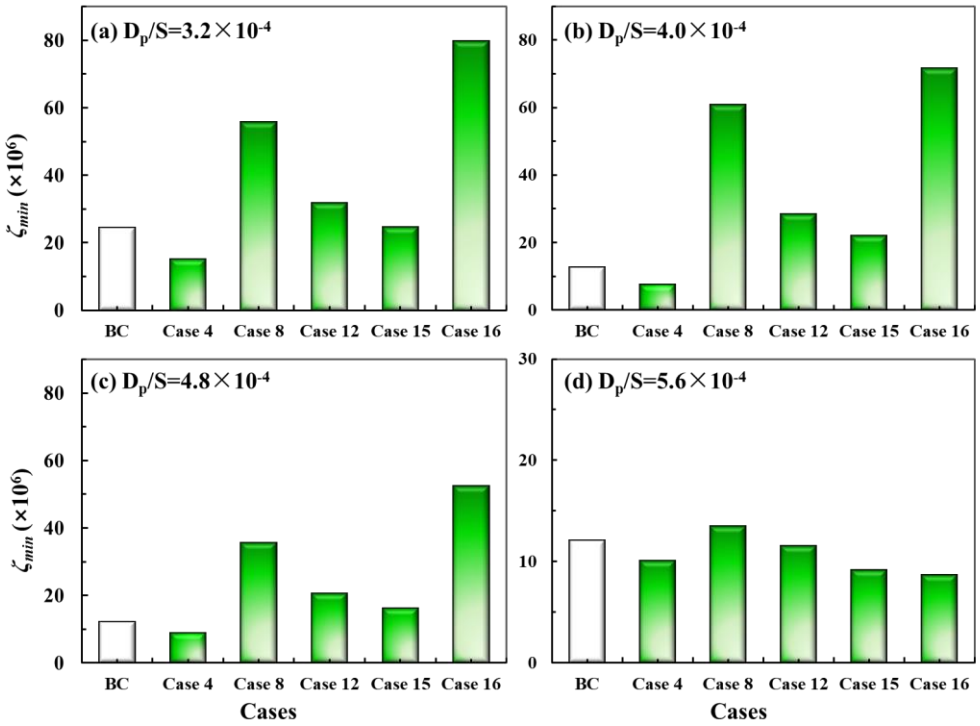

Fig. 11: Distributions of the ζ_{min} for the selected cases under various dimensionless droplet diameters (D_p/S={3.2×10^{-4}, 4.0×10^{-4}, 4.8×10^{-4}, 5.6×10^{-4}}).

Fig. 12 shows the minimum Reynolds number under varied dimensionless droplet diameters. As shown, for all the selected cases, the values of Re_{min} decline with the

increment of the droplet size. This can be explained by the fact that for relatively larger droplets, a lower value of gas velocity is required to separate all droplets from the gas flow. Meanwhile, the baseline case requires the highest Re_{min} (3.87×10^{3}), which is almost 2.2 times higher than that of Case 4 at D_p/S $=4.8\times10^{-4}$, followed by Case 16 (Re_{min} $=3.52\times10^{3}$) and Case 8 ($Re_{min}$$=3.17\times10^{3}$). In contrast, Case 4 with the optimal geometry has the lowest values of Re_{min} when D_p/S is larger than 3.0×10^{-4}, which implies that the Case 4 could attain the same separation efficiency by using a lower gas velocity as compared to other cases in a cooling tower application.

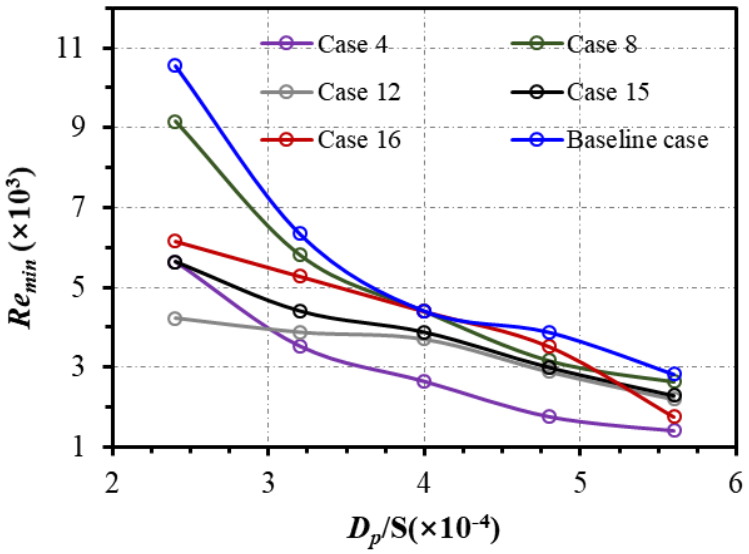

Fig. 12: The Re_{min} versus the dimensionless droplet diameter (D_p/S).

From the aforementioned comparison, it is concluded that Case 4, with a balanced performance of pressure drop and separation efficiency, could be considered as the best solution to the wave-plate mist eliminator. The optimized dimensional configurations of Case 4 can significantly strengthen the turbulence of the air stream and disturb the initial directions of movement of droplets, which results in an enhanced ability of

droplets to separate from the air stream. In particular, it can be attributed to the geometry-related factors as follows: (1) it possesses the highest number of bends that would unavoidably enhance the probability of droplets impinging on the inner wall when flowing through a stenosis area of the mist eliminator. (2) It has the lowest level of wavelength of a single bend with a minimum radius of curvature. The droplets with large inertia have a better ability to detach from the airflow since they cannot change their direction of movement rapidly with the airflow. (3) Case 4 has the highest level of W_2/S which produces a relatively low-pressure drop and less energy consumption.

4 Conclusions

This study combined the Taguchi experimental design, CFD simulation, and FAHP methods to obtain the optimal geometric design of a wave-plate mist eliminator. In the first step, the Taguchi experimental design was used to generate a manageable size of design cases based on the determined geometric parameters and levels of the baseline design. By integrating the SST κ-ω with the DRW model, the behaviour of multi-phase airflow inside the mist eliminator was well-described by the proposed two-dimensional CFD model. Through a batch of CFD simulations, the droplet separation efficiency and the associated pressure drop for all the 16 design cases were further estimated to provide the required data for FAHP. After that, five design cases were selected by the FAHP method due to their high GMIR scores. Further investigation showed that Case 4 possessed a balanced performance of separation efficiency (93.66%) and pressure drop (208 Pa) and could be regarded as the best solution to the design of a wave-plate

demister. In summary, the results highlighted the performance of the wave-plate mist eliminator was mainly affected by its geometric parameters, especially the bends number and the dimensionless width.

Acknowledgements

Financial support from the National Natural Science Foundation of China (No. 51776228) and the Science and Technology Planning Project of Guangzhou City, China (No. 201704030136) is gratefully acknowledged.

Nomenclature

C_D Drag force coefficient

C_L Integral time-scale constant

C_{pl} Pressure drop coefficient

CR_c Consistency ratio of matrices B_1/B_2

CR_w Consistency ratio of matrix A

D_p Particle diameter (μm)

D_ω Cross-diffusion term ($kg \cdot m^{-3}s^{-2}$)

F_D Coefficient in Drag force acceleration (s^{-1})

F_x Additional acceleration (N)

G_κ Generation of κ ($kg \cdot m^{-1}s^{-2}$)

G_ω Generation of ω ($kg \cdot m^{-3}s^{-2}$)

L_h Length of drainage channel (mm)

n Number of bends

Re_r Relative Reynolds number

RI	Random index
S	Channel width (mm)
St	Stokes number
T_L	Integral time scale (s)
u', v', w'	Random velocity fluctuation
$\overline{u_i' u_j'}$	Reynolds stress tensor
u_i	Fluid Reynolds average velocity components ($m \cdot s^{-1}$)
v_g	Gas velocity ($m \cdot s^{-1}$)
v_p	Velocity of droplets ($m \cdot s^{-1}$)
W_2	Distance between the drainage plate and the wall of the demister (mm)
W_2/S	Dimensionless width
W_h	Width of drainage channel (mm)
w_i	Weighting (s) of criteria or design case
ΔP	Pressure drop (Pa)
$\mu_{\tilde{\theta}}(x)$	Membership functions
Y_κ	Dissipation of κ ($kg \cdot m^{-1} s^{-2}$)
Y_ω	Dissipation of ω ($kg \cdot m^{-3} s^{-2}$)
α	Wave plate angle (°)
Γ_κ	Effective diffusivity of κ
Γ_ω	Effective diffusivity of ω
ε	Dissipation rate ($m^2 \cdot s^{-3}$)
ζ	Dimensionless power consumption coefficient
η	Droplet separation efficiency (%)

κ Turbulence kinetic energy ($m^2 \cdot s^{-2}$)

λ Wavelength of a single bend (mm)

λ_{max} Largest eigenvalue

μ Dynamic viscosity ($Ns \cdot m^{-2}$)

μ_t Turbulent viscosity ($Ns \cdot m^{-2}$)

ξ Normally distributed random number

ρ_g Density of gas ($kg \cdot m^{-3}$)

ρ_p Density of particle ($kg \cdot m^{-3}$)

σ_κ Turbulent Prandtl number of κ

σ_ω Turbulent Prandtl number of ω

τ_e Eddy life time

ω Specific dissipation rate of κ (s^{-1})

Subscripts

D Drag

g Gas

i,*j*,*k* Indexes

p Particle

References

Aguilar-Lasserre, A.A., Bautista, M.A.B., Ponsich, A., et al., 2009. An AHP-based decision-making tool for the solution of multiproduct batch plant design problem under imprecise demand. Comput. Oper. Res. 36, 711-736.

Ahn, B.S., 2017. The analytic hierarchy process with interval preference statements. Omega 67, 177-185.

ANSYS, 2019. ANSYS FLUENT Theory Guide, Release R1.

Bae, S., Kim, S.H., Lee, J.H., 2020. An investigation into the hydrodynamics of a spinning cone column: CFD simulations by an Eulerian-Lagrangian approach. Comput. Chem. Eng. 132, 106635.

Fang, C., Zou, R.J., Luo G.Q., et al. 2021. CFD simulation design and optimization of a novel zigzag wave-plate mist eliminator with perforated plate. Appl. Therm. Eng., 184, 116212.

Deng, H., 1999. Multi-criteria analysis with fuzzy pairwise comparison. Int. J. Approx. Reason. 2, 726-731.

Estakhrsar, M.H., Rafee, R., 2016. Effects of wavelength and number of bends on the performance of zigzag demisters with drainage channels. Appl. Math. Model. 40, 685-699.

Fadhila, H., Medina, H., Aleksandrova, S., et al., 2020. A new non-linear RANS model with enhanced near-wall treatment of turbulence anisotropy. Appl. Math. Model. 82, 293-313.

Feng, G., Lei, S., Guo, Y., et al., 2020. Optimisation of air-distributor channel structural parameters based on Taguchi orthogonal design. Case Stud. Therm. Eng. 21, 100685.

Gao, W., Li, Y., Kong, L., 2017. Numerical investigation of erosion of tube sheet and tubes of a shell and tube heat exchanger. Comput. Chem. Eng. 96, 115-127.

Galletti, C., Brunazzi, E., Tognotti L., 2008. A numerical model for gas flow and droplet motion in wave-plate mist eliminators with drainage channels. Chem. Eng. Sci., 63, 5639-5652

Ghetti, S., 2003. Investigation of entrainment phenomena in inertial separators. University of Pisa, Pisa, Italy.

Gottipati, R., Mishra, S., 2010. Process optimization of adsorption of Cr(VI) on activated carbons prepared from plant precursors by a two-level full factorial design. Chem. Eng. J. 160, 99-107.

Guo, S., Zhao, H., 2017. Fuzzy best-worst multi-criteria decision-making method and

its applications. Knowl. Based. Syst. 121, 23-31.

Kavousi, F., Behjat, Y., Shahhosseini, S., 2013. Optimal design of drainage channel geometry parameters in vane demister liquid–gas separators. Chem. Eng. Res. Des. 91, 1212-1222.

Koopman, H.K., Köksoy, Ç., Ertunç, Ö., Lienhart, H., Hedwig, H., Delgado, A., 2014. An analytical model for droplet separation in vane separators and measurements of grade efficiency and pressure drop. Nucl. Eng. Des. 276, 98-106.

Li, S., Wang, P., Luo, X., et al., 2020. Numerical analysis of chevron demisters with drainage hooks in optimizing separation performance. Int. J. Heat Mass Transf. 152, 119522.

Liu, Y., Yu, D., Jiang, J., et al., 2017. Experimental and numerical evaluation of the performance of a novel compound demister. Desalination 409,115-127.

Morsi, S.A.J., Alexander, A.J., 1972. An investigation of particle trajectories in two-phase flow systems. J. Fluid Mech. 55, 193-208.

Narimani, E., Shahhoseini, S., 2011. Optimization of vane mist eliminators. Appl. Therma. Eng. 31, 188-193.

Odu, S.O., Koster, P., van der Ham, et al., 2016. Heat Transfer to Sub- and Supercritical Water Flowing Upward in a Vertical Tube at Low Mass Fluxes: Numerical Analysis and Experimental Validation. Ind. Eng. Chem. Res. 55, 13120-13131.

Ogundoyin, S.O., Kamil, I.A., 2020. A Fuzzy-AHP based prioritization of trust criteria in fog computing services. Appl. Soft. Comput. 97, 106789.

Ooi, J., Promentilla, M.A.B., Tan, R.R., et al., 2018. Integration of fuzzy analytic hierarchy process into multi-objective computer aided molecular design. Comput. Chem. Eng. 109, 191-202.

Pinilla, A., Berrio, J.C., Guerrero, E., et al., 2020. CFD modelling of the hydrodynamics in a filtration unit with rotating membranes. J. Water Process. Eng. 36, 101368.

Ren, J.Z., Ren X.S., Shen W.F., et al., 2020. Industrial system prioritization using the sustainability - interval - index conceptual framework with life - cycle considerations. AIChE J. 66, e16961.

Saaty, T.L., 1977. A scaling method for priorities in hierarchical structures. J. Math. Psychol. 15, 234-281.

Schwaab, M., Silva, F.M., Queipo, C.A., et al., 2006. A new approach for sequential experimental design for model discrimination. Chem. Eng. Sci. 61, 5791-5806.

Tang, Y., Xu, Y.T., He, C., et al. 2021. Experimental and numerical evaluation of the performances of type-C and three-segment demisters used in cooling towers. Can J

Chem Eng, DOI: 10.1002/cjce.24221.

Tian, L., Ahmadi, G., 2007. Particle deposition in turbulent duct flows—comparisons of different model predictions. J. Aerosol Sci. 38, 377-397.

Venkatesan, G., Kulasekharan, N., Iniyan, S., 2013. Influence of turbulence models on the performance prediction of flow through curved vane demisters. Desalination 329, 19-28.

Wang, F., Yeap, S.P., 2021. Using magneto-adsorbent for methylene Blue removal: A decision-making via analytical hierarchy process (AHP). J. Water Process. Eng. 40, 101948.

Wissmann, P.J., Grover, M.A., 2010. Optimization of a Chemical Vapor Deposition Process Using Sequential Experimental Design. Ind. Eng. Chem. Res. 49, 5694-5701.

Xie, X., He, C., Xu, T., et al., 2017. Deciphering the thermal and hydraulic performances of closed wet cooling towers with plain, oval and longitudinal fin tubes. Appl. Therma. Eng. 120, 203-218.

Xie, X., Liu, H., He, C., et al., 2019. Deciphering the heat and mass transfer behaviors of staggered tube bundles in a closed wet cooling tower using a 3-D VOF model. Appl. Therma. Eng. 161, 114202.

Xu, Y., Yang, Z., Zhang, J., 2017. Study on performance of wave-plate mist eliminator with porous foam layer as enhanced structure. Part I: Numerical simulation. Chem. Eng. Sci. 171, 650-661.

Yu, Z., Sun, C., Fang, J., et al., 2021. Water recovery efficiency improvement using the enhanced structure of the mist eliminator. Process Saf. Environ., 154: 433-446.

Zamora, B., Kaiser, A.S., 2011. Comparative efficiency evaluations of four types of cooling tower drift eliminator, by numerical investigation. Chem. Eng. Sci. 66, 1232-1245.

Zhao, J., Jin, B., Zhong, Z., 2007. Study of the separation efficiency of a demister vane with response surface methodology. J. Hazard. Mater. 147, 363-369.

Zhu, Q., Zhang, B., Chen, Q., et al., 2020. Model reductions for multiscale stochastic optimization of cooling water system equipped with closed wet cooling towers. Chem. Eng. Sci. 224.